Low-Profile Induced-Voltage Distance Ranger for Smart Contact Lenses

Chayanjit Ghosh, Alex Mastrangelo, Mohit Karkhanis, Adwait Deshpande, Aishwaryadev Banerjee, Hanseup Kim and Carlos H. Mastrangelo

Abstract: *Objective*: In this paper, we present a novel, low-profile, scleral-coil based, distance ranging system which is suitable for smart, accommodating contact lenses. *Methods*: We measure the induced emf between a set of four thin semi-circular coils patterned on flexible Kapton substrates that conform to the eyes' sclera. This induced emf is a function of eye gaze angles. The system then determines the distance from the eyes to the desired object via the triangulation of these eye gaze angles *Results*: Experiments on eyeball simulated tissue gels indicate an accurate prediction of object distance in the 0.1-15 D range with a 0.15 D RMS error and object direction in the -15 to 15-degree arc with 0.4-degree RMS error, respectively. The energy required was determined to be as low as 20 μJ per range reading. *Conclusion*: Experimental data shows that our proposed new method of eye-tracking and distance ranging system can accurately predict eye-gaze angles and object-distance, whilst using only 20 μJ per range reading. *Significance*: The high-accuracy, low-profile and reduced energy requirements of the proposed eye-tracking technique, make it suitable for applications in the vast field of adaptive optics such as smart contact lenses and other low-power vision corrective applications.

I. INTRODUCTION

Presbyopia or loss of focal accommodation is an age-related irreversible condition affecting the majority of adults older than 45 years. Presbyopia produces loss of image focus and blurry vision and visual impairment. Focal accommodation however can be restored using varifocal eyeglasses [1]–[3], or smart contact lenses [4]–[7] that adaptively change the lens power with object location to produce sharp in-focus images of the observed objects in the visual field. An essential parameter for varifocal vision correction is the distance or range between the observer eye and the object being observed.

Date of submission:07/02/2020. This work has been partially supported by the National Institutes of Health NIBIB 5U0EB023048 cooperative agreement and the National Science Foundation grant CNS-1932602. (Corresponding Author: Carlos H. Mastrangelo)

C. Ghosh is with the Department of Electrical and Computer Engineering, University of Utah.

A. Mastrangelo is with the Department of Computer Engineering, University of Washington.

M. Karkhanis, A. Deshpande, A. Banerjee are with the Department of Electrical and Computer Engineering, University of Utah.

H. Kim is with the Department of Electrical and Computer Engineering, University of Utah.

C. H. Mastrangelo is with the Department of Electrical and Computer Engineering, University of Utah, Salt Lake City, Utah 84112, USA. (email: carlos.mastrangelo@utah.edu)

The object range can be determined actively or passively. Active approaches determine the range by emitting a beam of light or sound from the observer which bounces back at the object thus returning some of the beam energy to the observer. The range can then be determined by measurement of the reflected signal angle with respect to the source or its time-of-flight from the source to the object and back to the observer [8]. Active range finders are widely utilized for many industrial applications but this technique requires a bright, narrow beam source of radiation, the farther the object is the more power is required for the beam. Therefore, active range finders are unsuitable for utilization in low-power environments that have little or no energy sources available.

Unlike active range finders, passive range finders do not require the emission of radiation. In passive range finders, the location and range of the object are determined from the location or angles of the object observed from two different locations. The shift in the object location on the image is referred to as parallax [9], [10]. The object parallax and distance can be determined using images from two cameras separated by a distance, or the use of passive phase detectors [11] for example, but these methods require knowledge of the object that the observer is looking at and significant amounts of energy spent on image processing. One can determine the range more simply by direct measurement of the observer eye gaze angles as shown in Fig. 1. The distances h and r are the horizon and range, respectively. These two distances can be determined by triangulation.

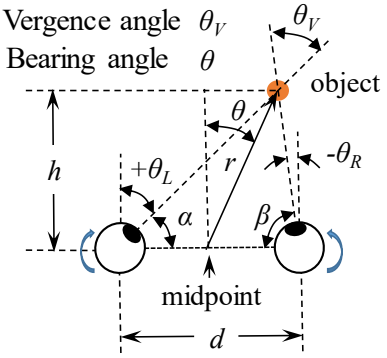

Fig. 1: Schematic of passive object distance ranging via triangulation from the eyeball angles α and β and the inter-pupillary distance d. Angles θ_L and θ_R are the left and right eyeball gaze angles, where $\theta_L=\pi/2-\alpha$ and $\theta_R=\beta-\pi/2$ and the object bearing angle $\theta=(\theta_L+\theta_R)/2$. The vergence angle is $\theta_V=(\theta_R-\theta_L)$.

Both distances are functions of the two steering angles α and β and the inter-pupillary distance d [12]

$$h = \frac{d}{(\cot(\alpha) + \cot(\beta))}, \qquad r = \frac{h}{\cos(\theta)} = \frac{d \cdot cos(\theta_R)\cos(\theta_L)}{\sin(\theta_L - \theta_R)\cos(\theta)} \tag{1}$$

When the eyes have verged on a target object, the vergence angle θ_V=(θ_R-θ_L) magnitude increases as the object comes closer to the eyes. When the object is far away ($d/r << 1$) and for small bearing angles ($\theta \approx 0$) the range can be approximated by the horizon. Typically, eyeballs are 24 mm in diameter and the inter-pupillary distance d is 60-70 mm. The angular rotation for the normal human eye is typically ±35 degrees [13], [14]. The gaze angle ranging scheme is attractive because it also automatically determines the direction of the object being observed.

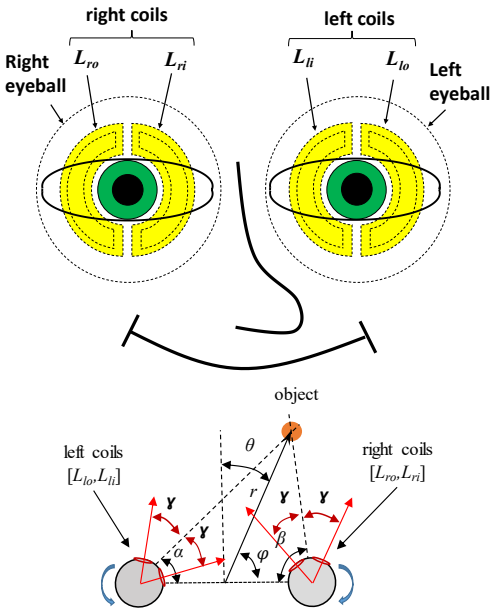

Fig 2: Schematic of the quad coil ranger. (a) Two semi-circular coils are symmetrically placed on each eye separated by angle 2γ. The coils in each eyeball are divided into inner and outer coils. (b) The range r is determined from the coils angle-dependent mutual inductance. The inner and outer radius of each semi-circular coil was 6 and 10 mm, respectively, and the eyeball is approximately 24 mm in diameter. The inter-pupillary distance was set to 60 mm for all the calculations.

Measurement of the eye steering angles (α,β) requires tracking of the observer's eyes. Eye-tracking can be performed in several ways[15]–[21] , including non-contact methods such as the use of cameras for pupil location [22], [23], Purkinje reflections [24], infrared reflections [25], [26] laser scanning [27], [28] and contact methods utilizing scleral coils [29]–[31]. Non-contact techniques use emission of light or imaging of the eyes hence require external difficulty to place or obstructing components and or require a significant amount of energy spent in the light emission. Contact techniques such as scleral coils methods require placement of components on the surface of the eyes.

Scleral coils are placed directly on the sclera (the white region) of the eyes and hence are very low profile with similar form factor as contact lenses. The main disadvantage of the conventional scleral coil method is that it requires a large external AC-driven electromagnet. The coils thus behave as the secondary winding of a transformer producing an electromotive force (EMF) voltage that is proportional to the cosine of the angle between the coil and the external field. The scleral coil method is regarded as the most precise contact method for eye tracking [29] with angle accuracy in the milli-degree range.

In this paper, we present a new contact technique based on the utilization of four coils placed on the sclera, two per eyeball. The new technique produces the magnetic field by one set of coils while the relative eye angle is determined from EMF voltage on the others. This eliminates the need for the external electromagnets. The entire ranger device thus has a low profile similar to a conventional pair of contact lenses. Additionally, the bulky components of the entire eye-tracking system such as the signal generator and the analyzer sub-system, can be also miniaturized by replacing them with commercially available ultra-thin, low-footprint and flexible electronic-systems; thus making our proposed eye-tracking system, suitable for integrating with varifocal contact lenses. In the sections below we describe the design of the system, the procedure used to determine the object direction and range from the induced coil EMF and experimental results.

II. OPERATING PRINCIPLE AND DEVICE MODEL

The objective of the new coil arrangement is the determination of the two eye angles α and β which uniquely determine the object range. Additionally, at least one of the coils must be responsible for the generation of a surrounding electromagnetic field. Therefore, a minimum of one generating coil and two receiving coils is required and to keep symmetry we have opted for a configuration with four coils that permits the angular measurement from either eye being the source of the field.

Fig. 2 shows the principle for the operation of a quad coils setup. Two non-obstructing conforming semi-circular coils are placed on the surface of the sclera surrounding the pupil, labeled as inner and outer coils, the inner coil being closest to the midpoint between the eyes. The coils are thus labeled as vector [L_{lo}, L_{li}, L_{ri} , L_{ro}]. When the observer eyes steer towards a particular object, the angle between the coils on the same eyeball remains constant, but the relative angles between the left eye coils and the right eye coils varies. The electromagnetic coupling between the left and right eyeball coils is also angle-dependent.

For example, if an electromagnetic field is generated by combining the two coils on the left eye together and we connect an AC signal generator such that their respective electromagnetic fields add up, the electromagnetic field generated by the left coils induces EMFs on the right eye inner and outer coils. Because these two EMF voltages depend nonlinearly with the angles α and β, it is possible to map the two

received voltages onto unique values of the gaze angles over some angular range of vision and the range from Eq. (1).

Electrical Equivalent Model

In essence the electrical equivalent of the ranger is a four coil, angle-dependent air transformer as shown in Fig. 3(a). The electrical behavior of this structure is described by its mutual inductance matrix *M(α,β)*. This is a 4x4 matrix dependent on angles α and β. This matrix has certain properties. First, all diagonal elements in *M* correspond to the coils self-inductances $L_i = L_o$, where L_o is a constant independent of the coil orientation and equal if the coils are identical.

Second, if the coils are identical the off-diagonal terms are symmetric as the coil coupling is identical if the signal is fed from the left coils into the right coils or vice versa. All of the angular dependence of $M(\alpha,\beta)$ originates from the non-diagonal elements.

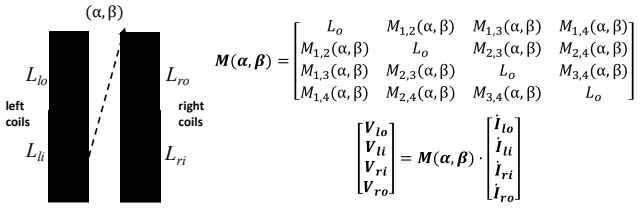

Fig. 3: Schematic of electrical equivalent quad coil system described by the mutual inductance matrix $\boldsymbol{M(\alpha,\beta)}$. The coil voltages are related to the derivative of the coil currents through this angle-dependent matrix.

The calculation of off-diagonal angular-dependent mutual inductance terms has been discussed elsewhere [32] for different coil shapes and angular configurations, and it is available in closed form for circular coils [33]. If the coils are not circular as in our device, there is no closed-form available, but if the distance between two coils is much larger than the coil diameter (as between left and right eye coils, for example), it can be approximated by the coupling of magnetic flux generated by the drive coil passing through the second receiving coil as shown in Fig. 4.

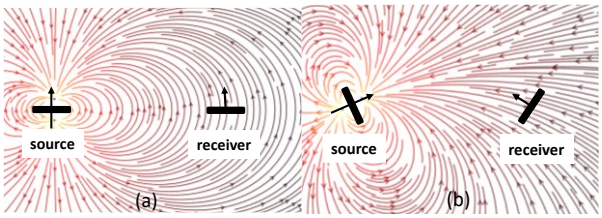

Fig 4: Magnetic dipole field produced by the source coil (a) if the receiving coil is parallel to the source the flux captured is maximum. (b) the captured flux is a function of coil separation and relative angle.

The mutual inductance is thus

$$M(\alpha,\beta) \approx \frac{\mu_o}{4\pi} \cdot A_s A_r N_s N_r \frac{[3 \cdot \hat{r}(\hat{r} \cdot \hat{n}_s) - \hat{n}_s] \cdot \hat{n}_r}{\|\vec{r}\|^3} \qquad (2)$$

Where μ_o is the vacuum permeability, A_s and A_r are the areas of the source and receive coils N_s and N_r are the number of turns of the source and receive coils, $\vec{r}$ is the vector from the center of the source coil to the center of the receive coil, $\hat{r}$ is the same normalized vector and $\hat{n}_s$ and $\hat{n}_r$ are the normals to the source and receive coils. Eq. (2) has a very nonlinear dependence on the relative coil orientation angles and a $||\vec{r}||^{-3}$ distance dependence. Eq. (2) can be utilized to determine much information about the relative magnitude of the off-diagonal terms. Since the distance between coils on different eyeballs is about three times larger than that the distance between two coils on the inside the same eyeball. Therefore, the eyeball-to-eyeball mutual inductance is at least 27 times weaker than the in-eyeball coil mutual inductance. Similarly, the distance between the two outer coils is about 1.7 times that between the two inner coils. This translates into a mutual inductance about 4.5 times larger between the two inner coils, and 2.4 times the mutual inductance between inner and outer coils of different eyeballs. The strongest off-diagonal mutual inductance term is between the two coils in the same eyeball and that is much less than the self-inductance. Therefore, the electromagnetic coupling between the source coil and all others is weak.

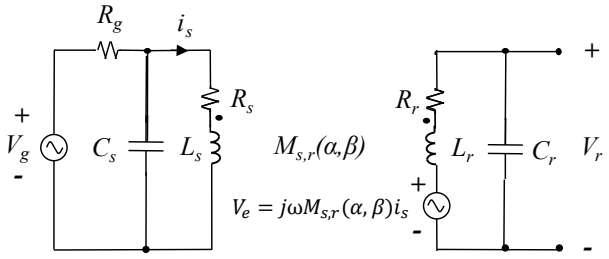

Fig 5: Approximate lumped equivalent circuit of source coil connected to a signal generator with series resistance R_g and cable of capacitance C_s. The source coil generating the magnetic field has series resistance R_s. On the receiving side, the receive coil has series resistance R_r, and it is connected to a line of capacitance C_r.

In order to obtain the object range distance and direction, one or more coils are connected to AC voltage generators and the electromotive force (e.m.f) on the remaining unconnected coils is measured. The induced e.m.f depends on several parameters including the AC frequency. Typically, the scleral coils used in this work use fine wires (~50 μm) and do not have many turns (5-15); hence the self-inductance is in the ~1 μH range, with resistances of 5-20 Ω and self-capacitance of a few pF.

Resonant Drive Characteristics

The coils produce maximum EMF when the source coils are matched with the generator at a specific resonance frequency [34]; therefore, operation of this device requires careful tuning for resonant frequency operation. Because of the weak coupling of signals in the mutual inductance matrix, the behavior of the system is basically dominated by the matrix diagonal; hence the drive coil characteristics are basically determined by the self-inductance of the driving source coils.

When a source coil is connected to a signal generator through a coaxial cable, the impedance of the connection cable must also be considered. If the cable length is smaller than ¼ of the wavelength inside the cable, impedance reflection effects can be neglected and the cable contribution to the circuit can be lumped. Furthermore, for short cables the cable inductance is much less than that of the coils; hence it can be neglected. Under the lumped impedance condition, the magnetic flux and the induced e.m.f is maximized when the system is driven at resonance, as shown in Fig. 5. The drive circuit has a characteristic resonance frequency:

$$\omega_r = \omega_o \sqrt{1 + \frac{R_s}{R_g}}, \quad \omega_o = \frac{1}{\sqrt{L_s C_s}} \tag{3}$$

If the receive coil capacitance is selected such that the receive side of circuit has the same resonance frequency as the source side, the receive coil circuit multiplies the induced e.m.f. represented by voltage source V_e in series with the receiving coil, by the quality factor of the receiving coil. For simplicity in this study, we consider only coil implementations where all four coils of the quad coil device are identical. For the case where L_s=L_r, R_s=R_r < R_g and $Z_s = (L_s/C_s)^{1/2} > R_g$, the magnitude of the received AC voltage at resonance is approximately

$$\|V_r\| \approx \frac{M_{s,r}}{L_s} \frac{\frac{1}{R_r}\sqrt{\frac{L_s}{C_s}}}{\sqrt{1 + \frac{C_s R_g R_s}{L_s}}} \cdot \|V_g\| \approx \frac{\omega_o M_{s,r}}{R_r} \cdot \|V_g\| . \tag{4}$$

In general, one obtains a larger receiver output voltage with a lower capacitance at the source and receiver ends corresponding to higher resonant frequency. The optimization of the output voltage for a given signal generator input at resonance is however, not simple, as the output increase caused by a larger mutual inductance M is accompanied with an increase in R_r that reduces the output voltage of the coils.

Eyeball Angles via Inverse Mapping and Orthogonality

For any valid eye ball angles α and β, two voltages are recorded $[V_A, V_B]$ corresponding to two different drive configurations, for example. This procedure defines a mapping vector function $[V_A, V_B] = \vec{F}([\alpha, \beta])$. Our goal is to find the specific drive and receive conditions such that the mapping vector function $\vec{F}()$ is invertible. In other words, we seek drive conditions such that $[\alpha, \beta] = \vec{F}^{-1}([V_A, V_B])$, is well defined and exists over a simply connected domain Ω in the $[V_A, V_B]$ plane. A fundamental requirement for inversion over a continuous domain is that at any given invertible point the Jacobian of $\vec{F}()$ is non-singular. This criteria essentially means that in vector space the functions $V_A = F_A(\alpha, \beta)$ and $V_B = F_B(\alpha, \beta)$ are not parallel to each other in the sense that the product of the zero-mean functions $f_A(\alpha, \beta) = F_A(\alpha, \beta) - \overline{F}_A$ and $f_B(\alpha, \beta) = F_B(\alpha, \beta) - \overline{F}_B$ such that $\iint_\Upsilon (f_A(\alpha, \beta) \cdot f_B(\alpha, \beta) d\Upsilon$ over the region Υ defined the specified (α, β) region is as close to zero as possible. This dot product defines an angle between the two signals $cos(\lambda) = f_A \cdot f_B / (||f_A|| \, ||f_B||)$. The coil drive and receive configurations for $[V_A, V_B]$ should be selected to make that angle as close to 90 degrees and orthogonality as possible. This angle also plays a role in the sensitivity of the inverse mapping to errors in the measurement of $[V_A, V_B]$. Locally, the Jacobian is a 2x2 matrix and the inverse Jacobian is inversely proportional to the determinant of the Jacobian and the sine of this angle. The closer this angle is to 90 degrees, the less susceptible the inverse map is to small errors in measurement of $[V_A, V_B]$.

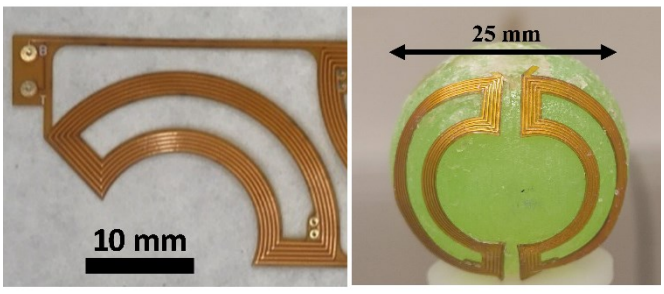

Fig 6: (left) photograph of a one thin, flexible, semi-circular coil constructed using a thin flex PCB process. (right) Photograph of two of these coils conformally mounted on a simulated eyeball.

III. COIL DESIGN AND FABRICATION

From the above discussion at resonance, it is evident from Eq. (4) that critical parameters for the coils are the mutual inductance to self-inductance ratio *M/L* and the coil resistance *R*. Maximization of the *M/L* ratio produces the maximum induced EMF at the receive coil while the coil series resistance reduces this signal. Two parameters maximize the *M/L* ratio. These are the coil turns *N* and coil area *A*. Since the coils must be unobtrusive, a semi-circular shape maximizes *A* and the space available for the coil winding. For a given coil area, increasing the number of turns increases *M/L* but the reduced width of the coil lines produces a higher coil resistance *R*, and the overall output decreases. Some of the signal drop can be compensated by using coils with thicker metallization if available. Due to its dependence on *R*, thin metal layers should be avoided for this application.

The semi-circular coils can be implemented in several flexible substrate technologies [35]. Many of these technologies, especially those implemented with thinner layers of metal, require the utilization of stress relief structures to prevent metal line fracturing and breaks when their corresponding substrates are subject to bending stresses. In our application, the space available is very limited and there is no room available for stress relief structures; hence we opted for a thicker metal, lower *R*, and less sensitivity to fracture technology offered by thin flex-PCB fabrication, which is readily available and inexpensive.

The semi-circular scleral coils are custom fabricated on a two-level copper wiring (~18 µm thickness) flexible PCB Kapton substrate about 100 µm-thick (Seeed Studio). Fig. 6 (left) shows a photograph of a single coil. Each semi-circular coil has 5 turns. The inner radius was 6 mm and the outer radius is 10 mm.

Note that the coil is fabricated in flat form; hence the angular span is < 180 degrees, but when mounted on a spherical surface the coil span becomes 180 degrees. The coil has a cutout in the middle to facilitate conforming the coil to a spherical surface. Each coil has a series resistance of ~6.4Ω, and an inductance of 1500 nH. Two of these coils were next mounted on a simulated eyeball. Fig 6(b) shows an example of these coils mounted on a 25.4 mm diameter rubber eyeball. The resulting coil mount is wrinkle-free. Each simulated eyeball has two of these coils. Two sets of eyeballs were fabricated and tested as discussed below.

IV. EXPERIMENTS AND DISCUSSION

The device's electrical and angular characteristics were tested for both frequency response and received voltage versus angular characteristics at resonance as discussed below.

Experimental Setup

Fig. 7 shows the experimental setup used. Two coils each are glued to two 25 mm polymer spheres that mimic the eyes. The spheres are placed at a distance of 60 mm to mimic the inter-pupillary distance between two eyes.

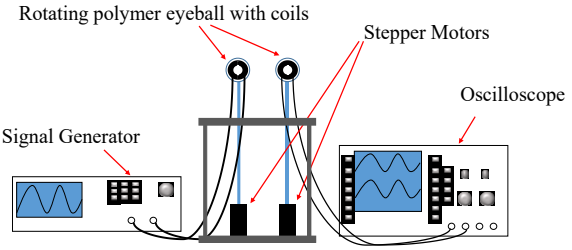

Fig 7: Schematic of the experimental setup with the source and receive coils

The balls are mounted on a long plastic shaft driven by a high precision stepper motor (Hitec D950 TW) having a resolution of less than 1 degree, providing precise angular positioning. The transmission coils are connected to a signal generator (Siglent SDG 2082x). We used spectrum analyzer (Siglent SSA 3021X) to find the resonance peak of the scleral coil system. The receiving coils are then connected to an oscilloscope (RIGOL DS 1074). The signal generator and the oscilloscope are connected to the computer through a USB connection. The signal generator was driven by a battery-powered inverter to minimize signal feedthrough through ground loops.

Phantom Tissue Mimic

We have used bovine gelatin to make phantom tissue mimic for the experiments, the gelatin has been sourced from Great Lakes Gelatin and Co. The gelatin used in this process is a type I gelatin, and during the manufacturing process, the collagen is extracted first, and then gelatin is made through the congealing process[36]. The phantom tissue mimic was made by mixing gelatin with water. Lukewarm water is poured on powdered bovine gelatin, and is stirred slowly until a uniform viscous mixture is formed. The viscous gelatin is then poured in a mold and is kept at ambient room temperature for setting. It takes about 24 hours for the gelatin mix to assume the shape of the mold. After that, it is removed from the mold and carved out appropriately to be used in the experimental setup. We observed that after prolonged exposure to air, the gelatin dries up and hardens, and sometimes deforms. To prevent this, the experimental setup is placed in an airtight container, where the humidity level of the air medium is maintained between 85 and 90% by a commercially available Vicks humidifier. The humidity level of the chamber is monitored continuously using a BME 280 humidity measuring chip, connected to an Arduino microcontroller.

Transfer Function Frequency Response

Using the setup of Fig. 7 we first set the two eyeballs such that they are facing forward and we connect the signal generator to the left eyeball inner coil while receiving the signal connected to a scope at the right inner coil. The capacitance of the coaxial lines connected to the generator and scope was about 150 pF and the signal generator resistance was 50 Ω. Fig. 8 shows the observed transfer function (T.F.) amplitude of the system $||V_r/V_g||$ versus frequency.

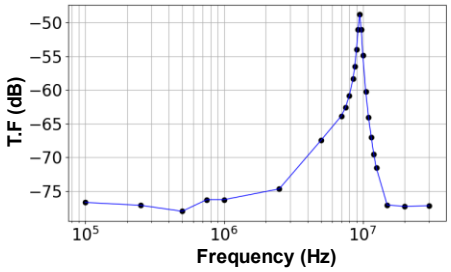

Fig 8: Amplitude of experimental transfer function $||V_r/V_g||$ vs drive frequency between the two inner coils of different eyeballs, with both eyeballs facing forward. The TF shows a single sharp resonant peak at about 10 MHz. The maximum value at resonance is -48 dB. The resonance is sharp with a Q of ~15.4.

The transfer function shows a sharp resonance at about 10 MHz with a maximum value of -48 dB. The Q of the observed resonance was about 15.4. Note the sharp drop off-resonance and the importance of the resonance operation mode. The flat regions of the curve are caused by a small amount of AC signal feeding through the setup external wiring. The higher the resonant frequency and Q are, the higher is the maximum value of the T.F.

Effect of Phantom Tissue

The same experiment was repeated in the presence of the tissue mimic phantom, showing a negligible influence of the mimic tissue. This is expected since the tissue does not materially affect the magnetic field produced by the source coil configuration, only affecting the resonance frequency slightly due to the presence of a slightly higher value of capacitances in the equivalent circuit of Fig. 5. Therefore, the following

experiments were measured without the phantom for simplicity in the setup.

Energy Requirements

A significant parameter of interest is the amount of energy required per range reading. To determine the energy required for this, we connected a 1 Ω resistance in series with the coil and applied a 20 V_{pp} voltage at resonance (~10 MHz). After typical circuit losses, the measured voltage drop across the coil at resonance was 14 V_{pp} and the voltage drop across the 1 Ω resistance is 0.1 V and is measured using a commercially available oscilloscope (Rigol DS1074). The current flowing through the coil was theoretically calculated to be ~76 mA, and the coil consumes a power of 1.064 W. If we utilize 100 cycles for each reading, we need to operate the system for 10 µs, therefore the total energy consumed per reading is ~ 11 µJ. Therefore, for two coils, the total energy consumption for a single reading is ~ 22 µJ.

Coil Configuration and Angular Response at Resonance

The angular response of the receiver coils was next characterized under different drive and receive coil conditions at resonance using the setup shown in Fig. 7. We performed the measurement when the signal generator was powered by AC power and when it was powered by a battery pack and inverter to check for the presence of direct feedthrough through ground loops. The measurements produced nearly identical results. A python code automates the rotation of the stepper motors over a combination of pre-defined gaze angles from -35 degrees to 35 degrees (70-degree freedom of horizontal movement)[13], [14], with a scanning resolution of 2.5 degrees from two different configurations that we label as A and B configurations.

The receive coil data has the form of two, two-dimensional voltage matrices V_A and V_B with elements $V_A(\alpha_i,\beta_j)$ and $V_B(\alpha_i,\beta_j)$. These matrices are discrete approximations of continuous functions $V_A(\alpha,\beta)$ and $V_B(\alpha,\beta)$. However, the source coil or coils drive condition, and the source and receive configuration is undetermined. However, we have made the following justified choices.

First, the magnitude of the receiver coil voltages is important. A higher EMF response is achieved when the source and receiver coils are closer. Therefore, the inner coil or the combination of inner and outer coils is used as a source configuration and the inner coil of the opposing eyeball as the receiver for $V_A(\alpha,\beta)$. Second, the response for $V_B(\alpha,\beta)$ must significantly differ from that of $V_A(\alpha,\beta)$. Eq. (2) suggests a very different response function is obtained if the angles from the source to the receiver coils in both configurations have a large angle difference. Therefore, we select a similar drive source coil configuration but a different receive coil, namely the outer coil of the opposing eyeball, which has an angle offset of 2γ respect to the inner coil. For any given configuration one can check how much different the two voltage signals are from each other by calculation of their relative angle λ in signal space.

We selected the following configurations in our experiments. For the A configuration, we utilized an AC voltage of 20 V_{pp} at resonance with the inner coil of one eyeball as the source and the inner coil of the opposing eyeball as the receiver coil. For the B configuration, we utilize an AC voltage of 20 V_{pp} on the outer coil and 20 V_{pp} on the inner coil of the same eyeball and recorded the received signal on the outer coil of the opposing eyeball. Scans were conducted with 841 points spanning from -35 to 35 degrees for α and β eyeball angles. Figs. 9(a) and (b) show their corresponding responses in air as a function of eyeball gaze angles [θ_L, θ_R].

The A configuration has a broad peak configuration symmetric around the θ_L=-θ_R corresponding to the two eyeballs converging to a point straight in front of the midpoint. The B configuration looks more like a plane. Huang et al [34], in their studies on the wireless power transfer efficiency on the tilt angles of the coils, have observed similar results. Some of the angle configurations for Fig. 9 are not converging and not physically meaningful.

The difference in the shape of these two signals can be observed in a more meaningful way when the scan is performed such that the points are recorded at a given range and the object bearing angle θ= (θ_L+θ_R)/2. The diopter object range is expressed a one over the range distance $D=1/r$, with units in diopters. These two plots are shown in Fig. 10 below.

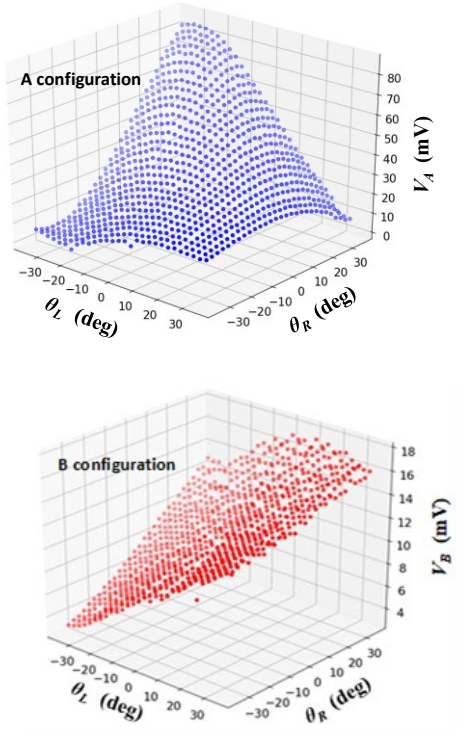

Fig 9: Induced RMS voltage recorded at resonance at the receive coils versus eye ball gaze angles in (a) the A, and (b) B configuration, in air. The average noise in these measurements was about 0.5 mV.

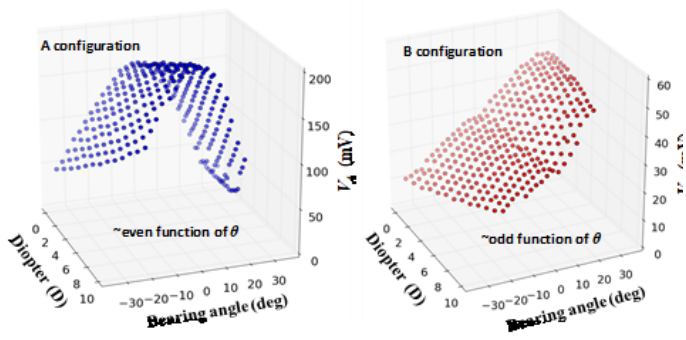

Fig 10: Receive coil voltages at resonance for the A and B configurations versus object diopter range D and bearing angle θ. The A configuration approximately even on θ, the B configuration is approximately odd with θ

Note that's these two signals are quite different from each other. The A configuration produces a generally even signal that is mostly dependent on the bearing angle and slightly increasing dependence on the diopter range. The B configuration produces a mostly odd signal dependent on bearing angle and slightly decreasing dependence on the diopter range. The odd and even observed configuration translates into an easier to invert the signal. The angle between these two configuration signals (subtracting the mean) computed in $[D,\theta]$ was 75 degrees indicating a good degree of orthogonality.

The discrete point data was used to construct continuous radial basis function (RBF) interpolation function of the inverse maps. These are shown in Fig. 11. The inverse maps work reasonably well for objects ranges between 0.1-10D, adequate for the restoration of the lost accommodation due to presbyopia.

The domain of the $[V_A, V_B]$ plane that produces valid gaze angles and object ranges can also be determined by plotting the experimental angles from Fig. 10 onto the $[V_A, V_B]$ plane. This is shown in Fig. 12 below. The region is simply connected and "smile-shaped", which follows the outline of the bearing angle projection onto the $[V_A, V_B]$ plane.

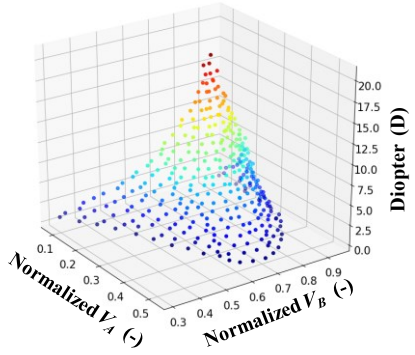

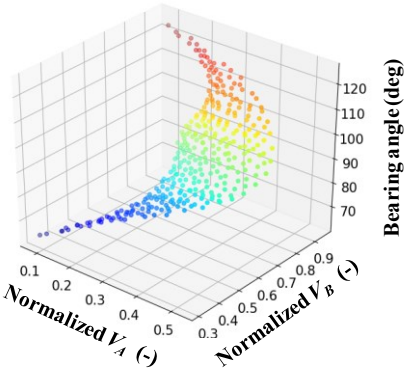

Fig 11: Inverse mapped RBF interpolation of the range and bearing angles from $[V_A, V_B]$.

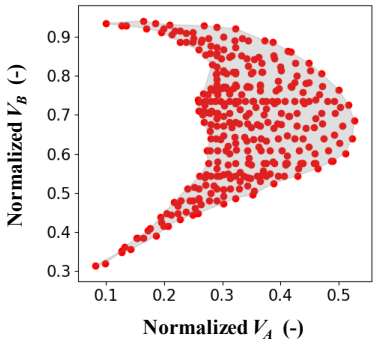

Fig 12: Normalized domain (grey region) of $[V_A, V_B]$ that produces valid diopter range points. Note that the region has a smile-like shape. Experimental values of $[V_A, V_B]$ that fall outside this domain are not valid.

Using the RBF inverse functions from Fig. 11 we also determined the correlation between actual range and diopter and the inverse mapped values. Figs 13 and 14 shows plots of the RBF-inverse predicted bearing angle and range in diopters, at the grid of scanned points and in between the scanned points compared to the actual bearing angles and range.

In Fig. 13, a straight unity slope line fits the data points with some data points distribution along the axis, the distribution of data points is observed to be minimal for negative bearing, i.e. for drive closer to the object than the receiver, and tends to scatter more for positive bearings. The RMS error from the bearing prediction is 0.48 degree, which is more than adequate for this application.

Fig. 14 shows the range prediction for positive bearing angles. The range prediction has an RMS error of 0.145 D. This is acceptable as for the average human observer the eye has an RMS aberration error of 0.35 D. The error was larger for negative bearings. The larger error is associated with a lower B signal as shown in Fig. 10, which yields a lower signal to noise ratio. For accurate predictions, in this configuration, the bearing direction should be first determined, and if negative, the opposing eyeball measurement should be performed to determine the range. Additionally, one may improve the

accuracy with the utilization of lower resistance coils with thicker metal layers which produce larger recorded signals.

V.CONCLUSION

We present a new method of distance ranging for contact lenses, by mutual induction of quad scleral coils. Scleral coils of different turn numbers were fabricated on a flexible polyamide substrate and mounted on simulated eyeballs. The signals emitted by a set of coils on one eyeball and received by the coils on the opposing eyeball are indicators of the eyeball gaze angles, from which the object range is determined. The ranger requires as little as 20 µJ energy expenditure per range reading and provides a range prediction with a standard deviation error < 0.25 D over a -15 to +15 degree field of view. The low energy requirement of the quad scleral coils makes it attractive for the distance ranging methods in smart contact lens and other low-power vision corrective optics applications.

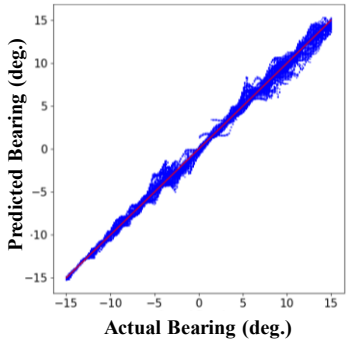

Fig 13: Predicted vs actual bearing angle of 56000 randomly distributed points that fall inside the valid domain region of Fig. 12. The standard deviation is lower for negative angles. The standard deviation of the prediction error was 0.47 degrees.

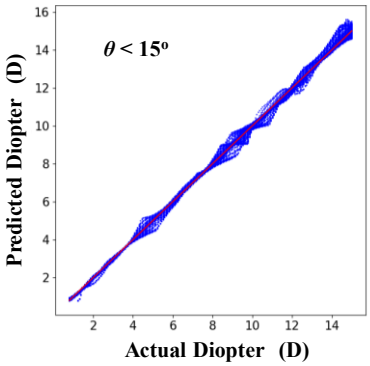

Fig 14: Predicted vs actual diopter range for 26000 randomly distributed points that fall inside the valid domain region of Fig. 12 for positive bearing angles less or equal than 15-degrees. The standard deviation of the prediction error was 0.145D. The standard deviation for negative angles is larger.

ACKNOWLEDGEMENTS

The authors would like to thank Erfan Pourshaban and Rugved Likhite for their help and invaluable suggestions.

REFERENCES

[1] N. Hasan *et al*, "Lightweight smart autofocusing eyeglasses," in *MOEMS and Miniaturized Systems XVII*, 2018, vol. 10545, pp. 26–31, doi: 10.1117/12.2300737.

[2] N. Hasan et al, "Adaptive optics for autofocusing eyeglasses," *Opt. InfoBase Conf. Pap.*, vol. Part F45-I, pp. 2016–2018, 2017, doi: 10.1364/AIO.2017.AM3A.1.

[3] N. Hasan et al, "Tunable-focus lens for adaptive eyeglasses," *Opt. Express*, vol. 25, no. 2, p. 1221, 2017, doi: 10.1364/oe.25.001221.

[4] Y. L. Liang and S. B. Jia, "Clinical application of accommodating intraocular lens," *Int. J. Ophthalmol.*, vol. 11, no. 6, pp. 1028–1037, 2018, doi: 10.18240/ijo.2018.06.22.

[5] H. E. Milton et al , "Electronic liquid crystal contact lenses for the correction of presbyopia," *Opt. Express*, vol. 22, no. 7, p. 8035, 2014, doi: 10.1364/oe.22.008035.

[6] J. Bailey et al , "Switchable liquid crystal contact lenses for the correction of presbyopia," *Crystals*, vol. 8, no. 1, 2018, doi: 10.3390/cryst8010029.

[7] J. F. Algorri et al, "Recent advances in adaptive liquid crystal lenses," *Crystals*, vol. 9, no. 5, pp. 1–20, 2019, doi: 10.3390/cryst9050272.

[8] P. Padmanabhan *et al*, "Modeling and analysis of a direct time-of-flight sensor architecture for LiDAR applications," *Sensors (Switzerland)*, vol. 19, no. 24, pp. 1–27, 2019, doi: 10.3390/s19245464.

[9] M. J. Carlotto, "Detecting change in images with parallax," *Signal Process. Sens. Fusion, Target Recognit. XVI*, vol. 6567, p. 656719, 2007, doi: 10.1117/12.721148.

[10] D. E. Simanek, "Images and Parallax." [Online]. Available: https://lockhaven.edu/~dsimanek/scenario/images.htm.

[11] K. Adi and C. E. Widodo, "Distance Measurement With a Stereo Camera," *Int. J. Innov. Res. Adv. Eng.*, vol. 11, no. 11, pp. 24–27, 2017, doi: 10.26562/IJIRAE.2017.NVAE10087.

[12] B. K. P. Horn, *Robot Vision*. Cambridge,MA: MIT Press, 1986.

[13] F. J. McGuigan and J. L. Andreassi, *Psychophysiology -- Human Behavior and Physiological Response*, vol. 94, no. 2. Psychology Press, 1981.

[14] N. & Associates, "Human Vision During the Walking Process," *Visual Acuity & Line of Sight*, 2010. [Online]. Available: http://www.hazardcontrol.com/factsheets/humanfactors/visual-acuity-and-line-of-sight.

[15] A. T. Duchowski, *Eye Tracking Methodology*. 2017.

[16] M. Horsley et al, "Current trends in eye tracking research," *Curr. Trends Eye Track. Res.*, pp. 1–345, 2014, doi: 10.1007/978-3-319-02868-2.

[17] K. H. N. A. D. H. van de Weijer, *Eye Tracking : A Comprehensive Guide to Methods and Measures*. Oxford University Press, 2011.

[18] J. N. Van Der Geest and M. A. Frens, "Recording eye movements with video-oculography and scleral search coils: A direct comparison of two methods," *J. Neurosci. Methods*, vol. 114, no. 2, pp. 185–195, 2002, doi: 10.1016/S0165-0270(01)00527-1.

[19] F. Träisk *et al*, "A comparison between the magnetic scleral search coil and infrared reflection methods for saccadic eye movement analysis," *Graefes Arch. Clin. Exp. Ophthalmol.*, vol. 243, no. 8, p. 791—797, Aug. 2005, doi: 10.1007/s00417-005-1148-3.

[20] A. Duchowski, "Eye Tracking Techniques," in *Eye Tracking Methodology*, 2017, pp. 51–59.

[21] D. L. Kimmel *et al*, "Tracking the eye non-invasively: Simultaneous comparison of the scleral search coil and optical tracking techniques in the macaque monkey," *Front. Behav. Neurosci.*, vol. 6, no. August, pp. 1–17, 2012, doi: 10.3389/fnbeh.2012.00049.

[22] F. Rynkiewicz *et al*, "Pupil Detection Methods for Eye Tracking," *J. Appl. Comput. Sci.*, vol. 26, no. 2, pp. 201–211, 2018.

[23] T. Santini *et al*, "PuRe: Robust pupil detection for real-time pervasive eye tracking," *Comput. Vis. Image Underst.*, vol. 170, pp. 40–50, 2018, doi: 10.1016/j.cviu.2018.02.002.

[24] M. R. Clark, "A two-dimensional Purkinje eye tracker," *Behav. Res. Methods Instrum.*, vol. 7, no. 2, pp. 215–219, 1975, doi: 10.3758/BF03201330.

[25] H. C. Kim *et al*, "Eye detection for gaze tracker with near infrared illuminator," *Proc. - 17th IEEE Int. Conf. Comput. Sci. Eng. CSE 2014, Jointly with 13th IEEE Int. Conf. Ubiquitous Comput. Commun. IUCC 2014, 13th Int. Symp. Pervasive Syst.* , pp. 458–464, 2015, doi: 10.1109/CSE.2014.111.

[26] Alexander S. Mastrangelo *et al*, "A Low-Profile Digital Eye-Tracking Oculometer for Smart Eyeglasses," in *2018 11th International Conference on Human System Interaction (HSI)*, 2018, pp. 506–512, doi: 10.1109/HSI.2018.8431368.

[27] C. K. Sheehy et al , "High-speed, image-based eye tracking with a scanning laser ophthalmoscope," *Biomed. Opt. Express*, vol. 3, no. 10, p. 2611, 2012, doi: 10.1364/boe.3.002611.

[28] C. K. Sheehy et al, "Active eye-tracking for an adaptive optics scanning laser ophthalmoscope," *Biomed. Opt. Express*, vol. 6, no. 7, p. 2412, 2015, doi: 10.1364/boe.6.002412.

[29] *Eric Whitmire et al*, "EyeContact," pp. 184–191, 2016, doi: 10.1145/2971763.2971771.

[30] A. Plotkin et al, "Magnetic tracking of eye motion in small, fast-moving animals," *IEEE Trans. Magn.*, vol. 44, no. 11 PART 2, pp. 4492–4495, 2008, doi: 10.1109/TMAG.2008.2002187.

[31] D. A. Robinson, "A Method of Measuring Eye Movemnent Using a Scieral Search Coil in a Magnetic Field," *IEEE Trans. Bio-medical Electron.*, vol. 10, no. 4, pp. 137–145, 1963, doi: 10.1109/TBMEL.1963.4322822.

[32] C. L. W. Sonntag *et al,*"Implementation of the Neumann formula for calculating the mutual inductance between planar PCB inductors," *Proc. 2008 Int. Conf. Electr. Mach. ICEM'08*, no. October, 2008, doi: 10.1109/ICELMACH.2008.4799978.

[33] S. S. Mohan et al, "Simple accurate expressions for planar spiral inductances," *IEEE J. Solid-State Circuits*, vol. 34, no. 10, pp. 1419–1420, 1999, doi: 10.1109/4.792620.

[34] W. Huang and H. Ku, "Analysis and optimization of wireless power transfer efficiency considering the tilt angle of a coil," *J. Electromagn. Eng. Sci.*, vol. 18, no. 1, pp. 13–19, 2018, doi: 10.26866/jees.2018.18.1.13.

[35] K. Takei, ed., *Flexible and Stretchable Medical Devices*, 1st ed. (Wiley-VCH Verlag GmbH & Co. KGaA, 2018).

[36] B. H. M. Goodsitt *et al*, "Angular distribution of scattered ultrasound from a single steel sphere in agar gelatin: A comparison between theory and experiment," vol. 347, pp. 342–347, 1984.